# Early-stage thermal performance design of thermo-active walls implemented in underground infrastructures

Jacopo Zannin [a,b,*], Alessio Ferrari [a,c], Pyrène Larrey-Lassalle [b], Lyesse Laloui [a]

[a] *Swiss Federal Institute of Technology in Lausanne, EPFL, Laboratory of Soil Mechanics, EPFL-ENAC-IIC-LMS, Station 18, 1015 Lausanne, Switzerland*
[b] *Nobatek/INEF4, 67 rue de Mirambeau, F-64600 Anglet, France*
[c] *Università degli Studi di Palermo, Engineering Department, Italy*

## ABSTRACT

Energy geostructures (EGs) represent an innovative technology in the sustainable energy agenda and are useful for satisfying the energy needs of the built environment. They are usually involving geostructures such as piles, walls, tunnels, shafts, and sewers. The application of such technology to infrastructure projects may have considerable thermal potential because of the large surfaces that can be thermally activated. This study focuses on thermo-active walls (energy walls, EWs), which are retaining structures used to sustain the sides of excavations. Key features related to their thermal design are examined, and a design methodology is proposed. The heat-exchange modes involving EWs and the surrounding materials (concrete, soil, air) are investigated via extensive three-dimensional hydrothermal finite-element simulations involving the non-isothermal flow in the heat exchangers (HEs), as well as all other heat-exchange modes. The results are first presented as charts related to the thermal behavior of the HEs under different hydrothermal environments. Finally, a methodology for early-stage thermal performance design is proposed, and a corresponding flowchart is presented. This study may be helpful for incorporating EGs into the engineering design.

© 2020 The Author(s). Published by Elsevier Ltd. This is an open access article under the CC BY-NC-ND license (http://creativecommons.org/licenses/by-nc-nd/4.0/).

## 1. Introduction

Geothermal energy is among the most important renewable and sustainable energy sources on Earth[1], and many different technologies exist for capturing this type of energy. This study focused on a particular type of shallow geothermal application: energy geostructures (EGs)[2]. EG, which are also called thermo-active geostructures, are innovative civil engineering geostructures that couple the structural role with a heat exchanger role. The transition from regular geostructures to EGs is simple, it only requires heat exchangers (HEs) to be installed and secured to the reinforcing cage whenever a new geostructure is needed. Some of the main advantages of this technology are that energy is continuously available, regardless of weather conditions, it is available almost everywhere and it is usable in a wide range of applications[3–10]. Possible applications of EGs and shallow geothermal systems include: (*i*) heating and cooling of civil engineering structures (residential and commercial buildings, industries, etc.)[11–14], (*ii*) production of hot water for agricultural needs[15–17], (*iii*) de-icing of deck, bridge and road pavements[18,19]. EG technology has been developed over the past decades[20] and exhibits a good potential for energy production[11], enabling the satisfaction of the heating and cooling needs of the built environment.

In this study, thermo-active walls, i.e., energy walls (EWs), are investigated. Typical examples of EW are single and multi-floored underground infrastructures (*e.g.,* train stations, underground car parks, and basements of high-rise buildings) and shallow cut-and-cover tunnels[21–27]. Among the various types of EGs, EWs represent a relatively new technology; consequently, numerous challenges exist. First, the heat transfer modes and the interactions between the EWs and the surrounding materials are not fully understood. Second, there is a lack of methods and guidelines for the thermal and mechanical analysis and design of EWs.

This study focused on the definition of the thermal performance of EWs. The objective was to develop a methodology for early-stage thermal performance design based on analysis of the hydrothermal behavior of EWs implemented in a one-level underground infrastructure. Herein, the main characteristics of the hydrothermal behavior of EGs that must be considered in the thermal performance design are first outlined. Second,

* Corresponding author at: Swiss Federal Institute of Technology in Lausanne, EPFL, Laboratory of Soil Mechanics, EPFL-ENAC-IIC-LMS, Station 18, 1015 Lausanne, Switzerland.
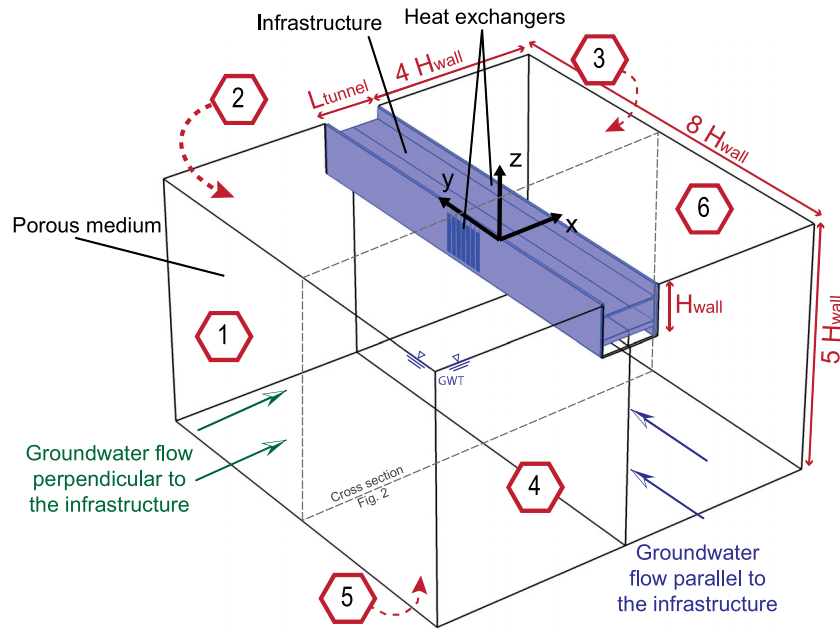*E-mail address:* jacopo.zannin@gmail.com (J. Zannin).

Fig. 1. View of the 3D model, indicating the boundaries: 1-left; 2-rear; 3-right; 4-front; 5-bottom; 6-top.

the features of a numerical model employed to investigate the hydrothermal behavior of EWs are presented. Then, the results of extensive numerical analyses (i.e., parametric analyses) are presented as charts that describe the thermal potential of installing EWs in different thermal environments and geometrical conditions. Finally, a design methodology with a sound theoretical basis that links the heat transfers, fluid dynamics, and seepage in porous media is developed and presented as a flowchart. This technique can easily be employed by designers to evaluate the thermal potential of EWs at a known site.

## 2. Materials and methods

### 2.1. Hydrothermal phenomena related to thermo-active walls

Thermal activation of walls and, more generally, of geostructures involves multiphysical phenomena interacting at two different scales: the infrastructure scale (i.e. lengths of $10^0$ to $10^3$ m), as reported and described by Ref. [28], and the HE scale. At the HE scale (i.e. lengths of $10^{-2}$ to $10^0$ m), a fluid flows in the pipes under non-isothermal conditions, and exchanges heat with the surroundings. Mutual, concurrent interactions between the two scales occur during thermal activation and affect the hydrothermal behavior. To thoroughly account for all such phenomena, three-dimensional (3D) hydrothermal finite element modeling is used in this study. To describe the thermal performance of EWs in different environmental and geometrical conditions, extensive numerical (parametric) analyses were performed, as described in the following sections.

### 2.2. Features of numerical analyses

In the analyses, a portion of an underground infrastructure was modeled using the finite element software Comsol Multiphysics©. The dimensions of the model along the x-, y-, and z-axes were as follows: $8H_{wall} + L_{tunnel}$, $8H_{wall}$, $5H_{wall}$, respectively (Fig. 1) where $H_{wall}$ represents the EW height and $L_{tunnel}$ is the tunnel width. The soil and concrete were considered as isotropic and homogeneous porous media. The soil was fully saturated by water. Six adjacent HE pipe loops[28] were modeled as linear entities embedded in the concrete walls.

The HE pipes had an outer diameter of 32 mm and an inner diameter of 25 mm. Water was selected as the circulating fluid, with the inflow velocity and temperature specified in Section 2.4. The pipe layout had a vertical W configuration.

The model formulation is reported in Annex A. The model mesh was created with the following features: (i) the HEs had a maximum mesh size of 10 cm; (ii) the infrastructure had a mesh size that ranged from 10 cm in the vicinity of the HEs to 1 m; (iii) the soil mesh was of 1 m in the vicinity of the EG and it increased with the distance from the underground infrastructure.

The analysis was divided between two solvers: the first was a stationary one, where the thermal and hydraulic boundary conditions were applied. The second was a time dependent solver, that took the solution of the stationary solver as the initial condition. The fluid flow in the pipes was enabled (i.e., geothermal activation) during the time-dependent solver. The details of the thermal input are specified in Section 2.4.

The model performance was first tested by reproducing the experimental test conducted at the Shanghai Natural History Museum[29]. The numerical model geometry presented in Fig. 1 was adapted to account for the experimental data reported for the Shanghai test[29,30]. All the model input data are reported in Annex B. The comparison results for the heat carrier fluid inflow ($T_{f,in}$) and outlet ($T_{f,out}$) temperatures reveal close agreement (Fig. 2).

Considering the complex geometry of the model (Fig. 1), various boundary conditions had to be set. Referring to the numbered boundaries in Fig. 1, thermal and hydraulic boundaries were set to account for two groundwater flow directions. Table 1 presents the selected conditions.

Here $H$ is the total hydraulic head, $\boldsymbol{n}$ represents the normal outflow unit vector, $\rho_w$ is the water density, $\dot{\boldsymbol{q}}$ represents the flow vector and $\dot{q}_{bc,i}$ represents the heat flux through the $i$th boundary. $T_{1,4}(z)$ is the temperature (°C) distribution along the depth ($z$, in meters) approximating the near-surface geothermal gradient in the shallower 10 m of the subsoil profile:
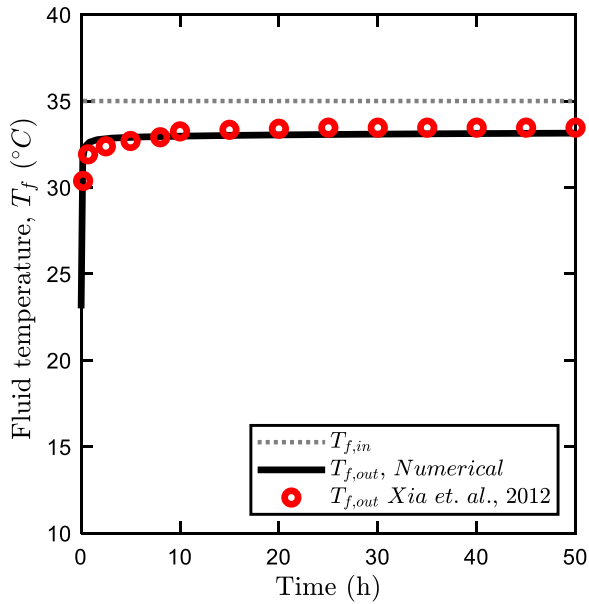
$$T_{1,4}(z) = \begin{cases} T_6 - z\dfrac{T_5 - T_6}{10 \text{ m}} & \text{for } 0 < z \leq -10 \text{ m} \\ T_6 & \text{for } z < -10 \text{ m} \end{cases} \qquad (1)$$

where $T_5$ and $T_6$ can be obtained from Table 2.

**Table 1**
Thermal and hydraulic boundary conditions (the numbered boundaries refer to Figs. 1, 3 and Table 2).

| Boundary nr. | Perpendicular groundwater flow | | Parallel groundwater flow | |
|---|---|---|---|---|
| | Hydraulic b.c. | Thermal b.c. | Hydraulic b.c. | Thermal b.c. |
| 1 | $H = -4$ m | $T_{1,4}(z)$ (Eq. (1)) | $\boldsymbol{n} \cdot \rho_w \boldsymbol{v_{rw}} = 0$ | $\dot{q}_{bc,i} = \boldsymbol{n} \cdot \dot{\boldsymbol{q}} = 0$ |
| 2 | $\boldsymbol{n} \cdot \rho_w \boldsymbol{v_{rw}} = 0$ | $\dot{q}_{bc,i} = \boldsymbol{n} \cdot \dot{\boldsymbol{q}} = 0$ | $H = \begin{cases} -7.5 \text{ m} \\ -11.0 \text{ m} \\ -18.0 \text{ m} \end{cases}$ | $\dot{q}_{bc,i} = \boldsymbol{n} \cdot \dot{\boldsymbol{q}} = 0$ |
| 3 | $H = \begin{cases} -5.25 \text{ m} \\ -6.5 \text{ m} \\ -9.0 \text{ m} \end{cases}$ | $\dot{q}_{bc,i} = \boldsymbol{n} \cdot \dot{\boldsymbol{q}} = 0$ | $\boldsymbol{n} \cdot \rho_w \boldsymbol{v_{rw}} = 0$ | $\dot{q}_{bc,i} = \boldsymbol{n} \cdot \dot{\boldsymbol{q}} = 0$ |
| 4 | $\boldsymbol{n} \cdot \rho_w \boldsymbol{v_{rw}} = 0$ | $\dot{q}_{bc,i} = \boldsymbol{n} \cdot \dot{\boldsymbol{q}} = 0$ | $H = -4$ m | $T_{1,4}(z)$ (Eq. (1)) |
| 5 | $\boldsymbol{n} \cdot \rho_w \boldsymbol{v_{rw}} = 0$ | $T_5$ (Table 2) | $\boldsymbol{n} \cdot \rho_w \boldsymbol{v_{rw}} = 0$ | $T_5$ (Table 2) |
| 6 | $\boldsymbol{n} \cdot \rho_w \boldsymbol{v_{rw}} = 0$ | $T_6$ (Table 2) | $\boldsymbol{n} \cdot \rho_w \boldsymbol{v_{rw}} = 0$ | $T_6$ (Table 2) |



**Fig. 2.** Model performance test: simulation of the Shanghai test[29] including a comparison between the experimental data and the numerical results.

**Table 2**
Boundary conditions (b.c.) at the wall–air interfaces (the names correspond to Fig. 3).

| Boundary details | | $T_{min}$ | $T_{max}$ | $v_{air,min}$ | $v_{air,max}$ |
|---|---|---|---|---|---|
| 5 | Bottom | 9 °C | 15 °C | – | – |
| 6 | Ground surface | 2 °C | 30 °C | 0 m/s | 5 m/s |
| 7 | Tunnel–air interface | 10 °C | 15 °C | 0 m/s | 5 m/s |
| 8 | Superstructure–air interface | 18 °C | | 0 m/s | – |

where $h_{a,i}$ is the convective heat transfer coefficient, $T_{a,i}$ represents the temperature of the ith boundary, and $T_{ref}$ is the temperature of the porous medium at the wall–air interface.

It is difficult to describe and monitor the air environment in tunnels with rectangular cross sections[36], and there is a lack of monitored sites[21]. The air temperature in tunnels varies with respect to: the distance from the entrance region, the depth of the tunnel, the influence of the external temperature, the thermal energy released by the passage of trains, the energy dissipated by trains during braking, the crowding of train stations, and eventually the presence of a lighting system. In this study, the temperature values for the air in the tunnel were selected after a dedicated literature review on shallow train tunnels located in Germany, France, Austria and the United Kingdom[37–42]. The airflow velocity is directly related to the convective heat transfer coefficient[21]. The selected reference values in this study ranged between 2.5 W/m²/K and 25.0 W/m²/K.

Moreover, two other environments exchange heat with the EW: a portion of the superstructure and the ground surface (Fig. 3, see locations 8 and 6). At 8, the internal conditions of a building are simulated: the temperature is set as 18 °C accounting for "near-zero" airflow. At 6, the temperature ranges from 2 °C to 30 °C, aiming at encompassing various thermal environments typical of European climates including worst case scenarios defined as very cold and very hot climates (average temperatures in Helsinki, Finland[43] during winter and Palermo, Italy[44] during summer), and an average airflow velocity of 2.5 m/s is accounted. A summary is presented in Table 2.

To test the impact of each boundary condition on the thermal exploitation, a dedicated set of preliminary sensitivity analyses was performed, referring to the configurations presented in Table 3. For the analysis, $h_{a,i}$ at the tunnel level was set as 25.0 W/m²/K only.

Neglecting the heat exchanges between the wall and the air (Config. 1) may lead to a critical underestimation of the thermal potential. On the other hand, accounting for the heat exchanges on a portion of the superstructure may lead to overestimation of the thermal potential (Config. 4). In real applications, at shallow depths, the pipes may be thermally insulated to avoid major thermal losses in the top part of the excavation. Consequently, Config. 3 was adopted for the remainder of the study.

The hydraulic head boundary allows the undisturbed groundwater flow velocity ($v_{gw}$) to be set to different values. In this study $v_{gw}$ ranged from 0 m/d to 2 m/d[18,31–33]. Different wall geometries were examined: the total wall height varied between 25.5 m and 40.0 m. The height of the excavated zone remained as indicated in Fig. 3, while only the embedded height varied. This was chosen to satisfy the geotechnical requirements as from the Eurocode7[34]. According to this definition, the ratio ($r_w$) between the total wall height ($H_{wall}$) and the retained height ($H_r = 19.9$ m as shown in Fig. 3) ranged between $r_w = 1.28 \div 2.01$.

The thermal behavior of the EW may be significantly affected by the hydro-thermal interactions between the wall and the airflow in the tunnel[21,35]. In some conditions, the heat exchanged in this portion of the structure (i.e., at the wall–air interface) may be predominant: the combination between the air flow velocity and the tunnel air temperature defines the heat exchange. In finite element analyses, convective boundary conditions can be employed to describe this phenomenon, avoiding modeling the complete airflow circulation in the tunnel. This is a flux boundary condition described as follows:

$$\dot{q}_{bc,i} = \boldsymbol{n} \cdot \dot{\boldsymbol{q}} = h_{a,i} \left( T_{a,i} - T_{ref} \right) \qquad (2)$$
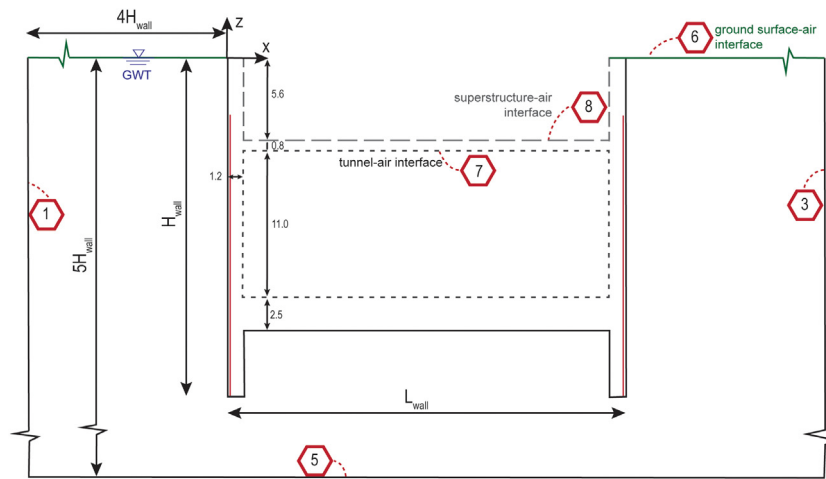
**Fig. 3.** Cross-sectional schematic indicating the boundaries (NOTE: the figure is not scaled, quotes are in meters).

**Table 3**

Configurations used for the comparison of the boundary conditions.

| Configuration | Description of the b.c. |
|---|---|
| Config. 1 | 6, 7, 8 thermally insulated |
| Config. 2 | 7 active, 6 and 8 thermally insulated |
| Config. 3 | 6, 7 active, 8 thermally insulated |
| Config. 4 | 6, 7, 8 active |

### 2.3. Properties of involved materials

The soil description was chosen to perform a thermal characterization typical of fine- and coarse-grained materials. From a hydraulic viewpoint, the chosen geometric permeability was the one typical for coarse-grained materials[28,33], as higher groundwater flow velocities are expected to occur for coarser materials. The infrastructure was made of concrete, and the HE pipes were made of high-density polyethylene (HDPE). Water was the circulating fluid inside the HEs and the saturating medium in the soil. The details are presented in Table 4.

A wide variety of hydro-thermal environments in the soil and at the air interfaces were simulated by varying several parameters (Table 5). The variations in the soil thermal conductivity ($\lambda_s$) aimed at encompassing the majority of shallow subsoil materials, whereas in the case of concrete ($\lambda_c$), the thermal conductivity varies in function of a number of parameters, such as the aggregate mix composition and water content (see Section 3.2).

### 2.4. Definition and choice of thermal input

The choice of the thermal input is crucial for defining the thermal behavior of the HE. The selected numerical model includes the convective and conductive heat transfers within the fluid, pipe material, concrete, soil and air. In a real application, the thermal input imposed by the heat pump to the primary circuit satisfies the (total or partial) energy demand of the served superstructure. Because this study deals with the preliminary design stages of a project, there are numerous challenges related to the selection of the thermal input.

First, a broad variety of energy demand curves exist for different types of civil engineering structures and shallow geothermal applications. It is difficult to define a reliable thermal input that is representative of all the possible conditions, for winter and summer operations. Second, the elements constituting the EG exhibit a response that differs with respect to time and space[45] depending on the material characterization and on the ongoing multiphysical phenomena, inducing mutual hydro-thermal interactions[28]. Third, accounting for a dynamic thermal input implies a high computational cost and large number of runs.

A trade-off can be achieved by using relatively short-time constant temperature inputs, to detect the response of the EG both in the transient and steady flux conditions, providing a comprehensive overview of the thermal behavior of the HE when either the short term (intermittent) or long term constant modes is selected[29]. With a constant temperature input, the thermal response of the HEs is linear depending on the inflow temperature (Fig. 4), but some correlations to the dynamic response can be pointed out. It is possible to evaluate the dynamic thermal behavior of the HE by applying the Duhamel principle: the dynamic problem can be solved by accounting for a sequence of infinitesimal impulses of different amplitudes, as shown in Ref. 45. Moreover, at the early stages of EG design, the energy demand curve may not yet be defined with sufficient accuracy. For these reasons, a constant with time temperature input was set. To account for temperature limits that are usually prescribed for EGs (*i.e.,* soil temperature to be maintained between 0 °C and 50 °C), the inflow temperature of the fluid ($T_{f,in}$) in the pipes was set at 5 °C and 25 °C for winter and summer operation, respectively, yielding an average temperature difference between the fluid in the pipes and the soil of $\mp 10$ °C, as shown in Fig. 4. The power extraction/injection rate ($\dot{q}$), expressed in W/m$^2$, of the HE loop can be quantified[10,46] as the enthalpy drop between the inflow and outflow sections:

$$\dot{q} = \frac{A_P \rho_f Cp_f v_f \Delta T_f}{A_W} \tag{3}$$

where $\rho_f$, $Cp_f$ and $v_f$ represent the density, heat capacity and velocity of the circulating fluid, respectively. $\Delta T_f$ is the fluid temperature difference between the pipe outflow and inflow, and $A_W$ is the equipped surface of the wall.

A constant fluid velocity of 0.5 m/s in the pipes was also applied to attain turbulent regime. The duration of the analyses was set to 50 d, which has proven to be sufficient to reach the steady flux domain.

## 3. Results and discussion

The results of the numerical analyses are presented in this section, with a focus on the HE scale and the thermal response of the HEs. The results are presented as charts corresponding to selected times, allowing the short-term and steady flux responses to be evaluated. The time dependent HE response is first described. Second, design charts aiming at highlighting the effects of soil

**Table 4**
Material properties.

|  | Material | Porosity $n$ (-) | Density $\rho_s$ (kg/m$^3$) | Geometric Permeability $k^*$ (m$^2$) | Heat capacity at constant pressure $C_p$ (J/(kg K)) | Thermal conductivity $\lambda$ (W/(m K)) |
|---|---|---|---|---|---|---|
| Soil | Coarse grained | 0.35 | 2735 | $10^{-10}$ | 890 | 1.5 to 3.5 |
| Structure | Concrete | 0.10 | 2722 | – | 837 | 0.7 to 2.0 |
| Pipes | HDPE | – | – | – | – | 0.4 |
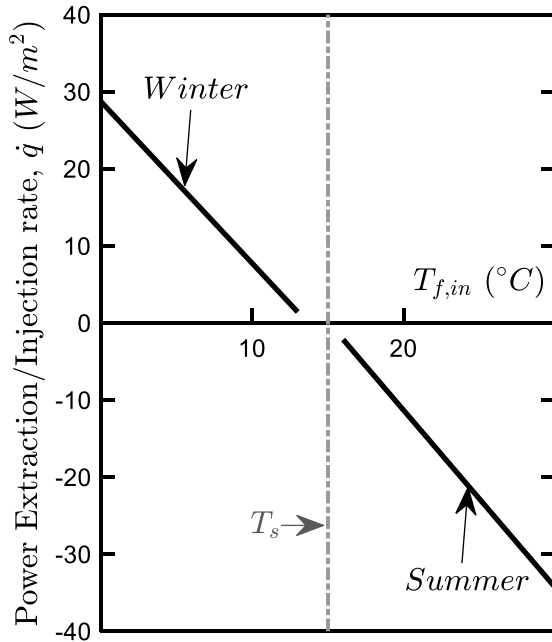


**Fig. 4.** Thermal response of a heat exchanger loop at a steady flux with a varying inflow temperature input.
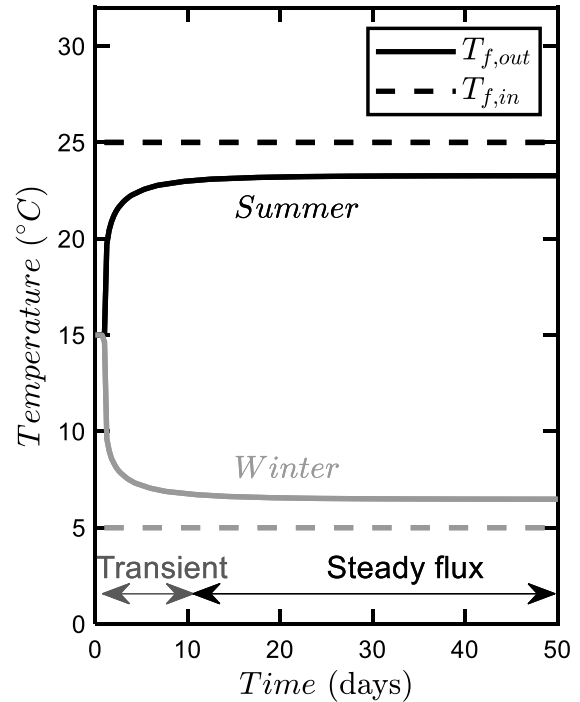


**Fig. 5.** Applied thermal input, indicating the heat transfer conditions.

thermal characterization are proposed. The subsequent section is dedicated to the structural thermal characterization. Additionally, a flowchart to be employed for early-stage thermal performance design is proposed. Table 5 presents the ranges of the parameters introduced in Section 2.2.

The HE's thermal response was evaluated accounting to the power extraction/injection rate using Eq. (3). A fluid velocity and a temperature were imposed at the pipe inlet, while the fluid temperature at the outflow was monitored. According to the time dependency of the thermal response of the HE to a constant thermal input (Section 2.4), two zones were defined (Fig. 5): (*i*) an initial, time dependent portion (the duration depending on the fluid velocity, the pipe loop length and shape) in which the heat exchanges were governed by the heat capacity and the thermal conductivities of the involved materials (called "transient"), and (*ii*) a time-independent phase where the heat exchanges were governed by the thermal conductivities of the materials only (steady flux).

Under transient conditions, the volume of materials affected by the heat flow quickly increases with time: the portion of soil affected by the thermal exchange was on the scale of decimeters to meters. The groundwater flow presence (if any) interacts with the increasing soil volume in which the heat exchange occurs. Because of this interaction, for the short-term response, the seepage may not significantly enhance the behaviors of the HEs. The impact of the groundwater flow on enhancing the heat transfer process increases as steady flux conditions are approached. Owing to the spatial evolution of the heat exchange processes in the soil, the power injection/extraction rate decreases with time. The temperature distribution in the soil was hence transient, and the heat front moved in the direction of the seepage[28].

Once the steady flux was reached, the thermal response of the HEs was time independent. This condition was reached after an activation time on the order of 10 d and allowed us to define and analyze long term energy exploitation scenarios[29]. The soil volume involved in the heat exchange reached its definitive evolution and was recorded on the scale of a few cubic meters around the EG. If groundwater flow is present, the soil volume affected by the thermal exchanges was significantly larger depending on the direction and magnitude of the seepage. In this condition, mutual interactions among the seepage and the HE occurred: on one hand, the seepage affected the heat exchanges by moving the heat in the space, and on the other hand, the thermal activation induced local seepage variations[28].

To study the time-dependent behavior of the HEs' response, three time steps were examined, with the aim of comprehensively evaluating the time-dependent heat transfer rates. The selected timesteps were: 2, 5, and 50 d. The first aimed at defining the short-term response (*e.g.* representing highly intermittent heat pump functioning), the second provided an average value for the transient condition, and the third provided a measure of the long-term seasonal performance.

*3.1. Thermal behavior of EG under different environmental conditions*

In the following section, charts (Figs. 6 and 7) show the power extraction/injection rate ($\dot{q}$, on the y axis) with respect to the groundwater velocity ($v_{gw}$, on x axis), for two different groundwater directions and soil thermal conductivities. In both cases,

**Table 5**
Ranges of the studied parameters.

|  | $\lambda_s$ | $\lambda_c$ | $T_5$ | $T_6$ | $T_7$ | $v_{gw}$ | $T_{f,in}$ | $H_{wall}$ |
|---|---|---|---|---|---|---|---|---|
| min | 1.5 W/m/K | 0.7 W/m/K | 9 °C | 2 °C | 10 °C | 0 m/d | 5 °C | 25.5 m |
| max | 3.5 W/m/K | 2.0 W/m/K | 15 °C | 30 °C | 15 °C | 2 m/d | 25 °C | 40.0 m |
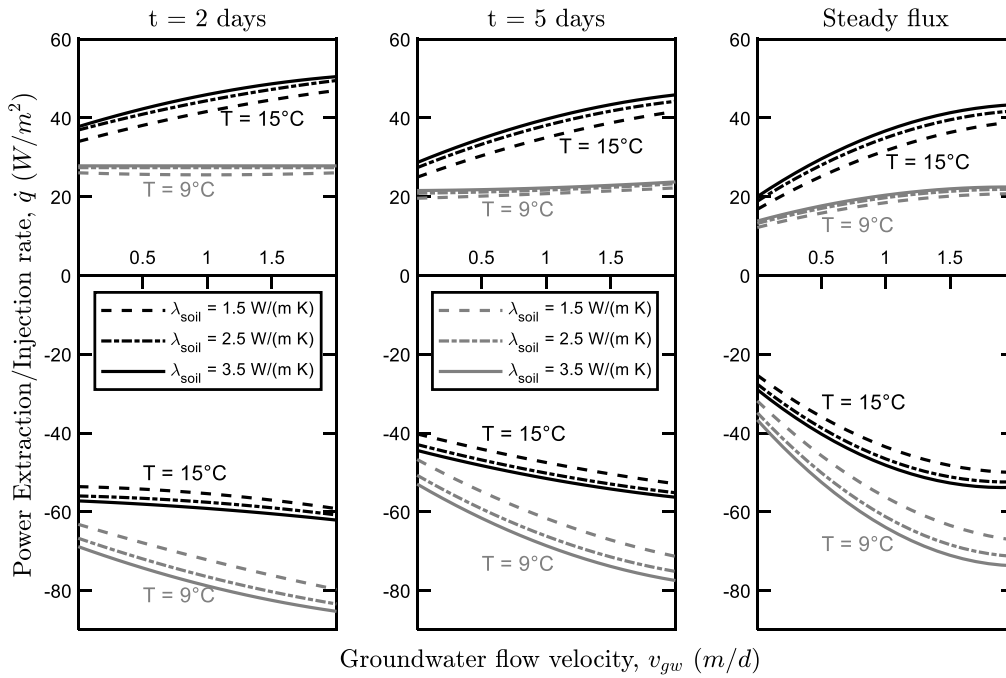


**Fig. 6.** Charts for groundwater flow parallel to the wall.
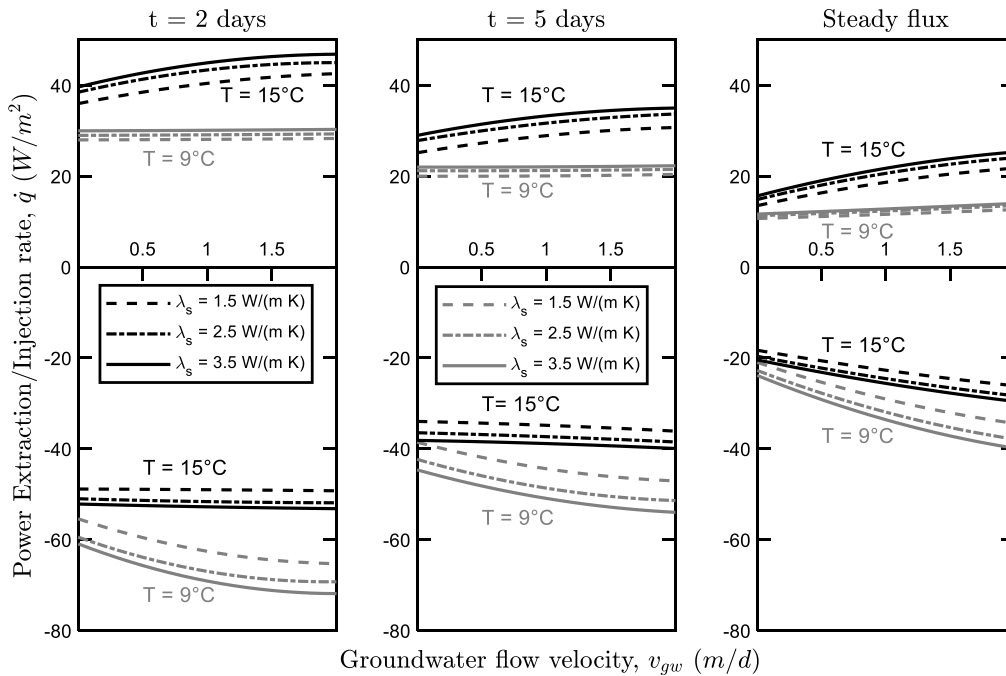


**Fig. 7.** Charts for groundwater flow perpendicular to the wall.

the results refer to the first pipe loop number (*i.e.,* the one with higher performance); hence all hydraulically induced thermal interactions are neglected. In the subsequent figures, all the results refer to a concrete thermal conductivity of 2.0 W/(m K). The

significance of this key parameter to the results is discussed in Section 3.2.

To illustrate the effect of increasing the number of HE loops, Fig. 8 shows the decrement of the power extraction/injection rate of adjoining HE loops for selected groundwater flow velocities
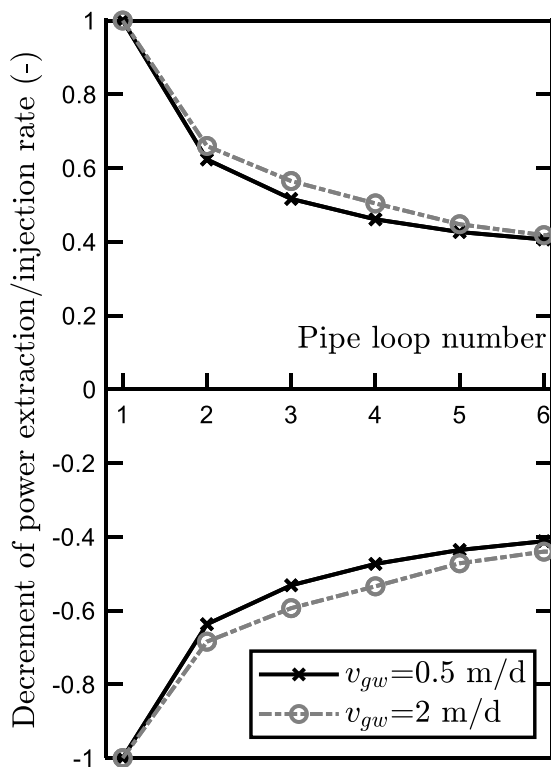
**Fig. 8.** Power extraction/injection rate of adjoining pipe loops in the case of groundwater flow parallel to the wall.

parallel to the wall. The choice to employ six HE loops was based on a literature review[28], which indicated that the thermal performance of the HEs remains constant after a certain number of HE loops.

Figs. 6 and 7 show the time-dependent decrease (absolute value) of the thermal performance (i.e., power extraction/ injection rate) for the HEs transitioning from transient to steady flux conditions. Notably, the thermal performance of the geostructure for the condition of groundwater flow parallel to the wall was higher than that for the corresponding with perpendicular groundwater flow conditions. This was expected, because the magnitude of $v_{gw}$ for the parallel flow was higher than that for the corresponding case with a perpendicular flow, owing to the seepage. In contrast, in the parallel flow case, hydraulically-induced thermal interactions among adjoining loops affected the thermal behavior, as shown in Fig. 8. Such results may be useful for a preliminary estimation of the energy potential achievable with the HEs embedded in retaining walls for early-stage thermal performance design of the EG. In Figs. 6 and 7, the symbol T indicates the undisturbed soil temperature (i.e., at the far field).

### 3.2. Effects of thermal characteristics of structure

The effect of the structural thermal characterization on the thermal behavior of the HEs is discussed in this section. The thermal properties of concrete (i.e., the structural material) are typically affected by seven parameters[47]: the humidity conditions, age, temperature, water-cement ratio, fine aggregate fraction, type of admixture, and total aggregate volume fraction. The moisture content and temperature are highly important: the thermal conductivity in saturated conditions is 50% higher than that in dry conditions[48]. Additionally, in experimental studies, the thermal conductivity increased by approximately 6% with each increment of 1% in the moisture content[49]. The aggregate type

is another important parameter because concrete is composed of aggregates for about 60% ÷ 80% of its volume. The thermal conductivity is increased by increasing the coarse aggregate volume fraction and keeping the sand ratio unchanged[48]. The density is another significant parameter: an increase in the density induces an exponential increase in the thermal conductivity[47].

The thermal conductivity of concrete can be engineered to some extent: for EG applications, one can choose a concrete type with better properties than alternatives, but the long-term soil–structure interactions and the implications for the thermal behavior are hardly definable at the design stage. They depend significantly on the hydro-thermal interactions among the materials. In the case of the EW, the interactions between the wall and the air on the excavated side and between the wall and the soil on the other side may locally affect the thermal properties of the structure. To consider such scenarios, in this study, the concrete thermal conductivity was varied from 0.7 W/(m K) to 2.0 W/(m K)[47]. Figs. 9 and 10 indicate the ranges of values of the power extraction/injection rate with respect to the groundwater flow velocity for different combinations of concrete and soil thermal conductivities. The charts correspond to the first pipe loop, and the hydraulically induced thermal interactions were not considered.

For each concrete thermal conductivity value, a surface was identified. The minimum and maximum (absolute) values for each surface corresponded to the low and high soil thermal conductivities, respectively.

### 3.3. A flowchart for early-stage thermal performance design

This section aims at linking the subsoil characteristics and environmental air conditions to the energy quantities achievable with EWs by defining a flowchart that can be used not only for the preliminary thermal design of EWs but also for the decision-making process to decide whether to employ EGs in an infrastructure project. The required input parameters are related to the basic hydro-thermal properties of the site: estimations of the thermal properties of the involved materials and the possible presence and velocity of groundwater flow that may significantly interact with the infrastructure. The flowchart comprises two steps. First, according to the fluid dynamics theory, the main heat exchange mechanism is defined. Second, by selecting the input thermal properties, thermal performance of HEs embedded in EWs is estimated. The objective of this section is to propose a design methodology for energy evaluations at preliminary design stages, to address a frequently asked question: how much energy is achievable by using this technology at a known site?

#### 3.3.1. Analytical solution and Péclet number for steady flux calculations

To recall some fundamentals of thermodynamics and fluid dynamics, a simple sketch of an EW was made by considering the case of a porous material constantly heated from the side by a rectangular heat source (Fig. 11(a)). In this condition (i.e., steady flux), it was possible to describe the heat transfer process (conduction and convection) analytically. The case of a porous medium fully-saturated with water, with the liquid phase moving at velocity $\bar{u}_x$, under two-dimensional (2D) conditions, is presented in Fig. 11(b). Under such conditions, we can determine in which cases the heat exchanges are dominated by conduction ($Pe < 1$) and convection ($Pe > 1$), according to the Péclet number ($Pe$). This dimensionless quantity is the ratio of the convective transport rate and the conductive transport rate in a continuum. When applied to hydro-thermal phenomena, it is equal to the product of the Reynolds ($Re$) and the Prandtl ($Pr$) numbers:

$$Pe = \frac{convective\ transport\ rate}{conductive\ transport\ rate} = Re\ Pr = \frac{\overline{vx}}{\alpha} \qquad (4)$$
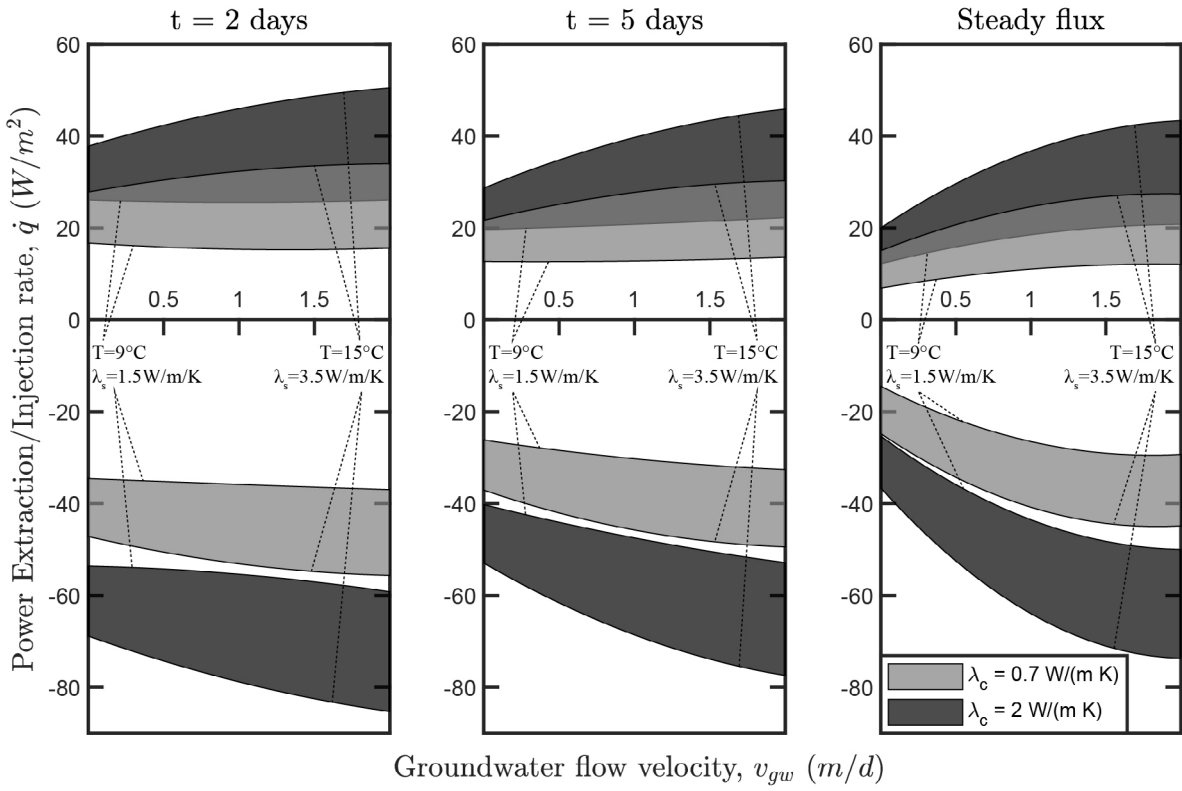
**Fig. 9.** Dependency of power extraction/injection rate on concrete thermal conductivity for groundwater flow parallel to the wall.
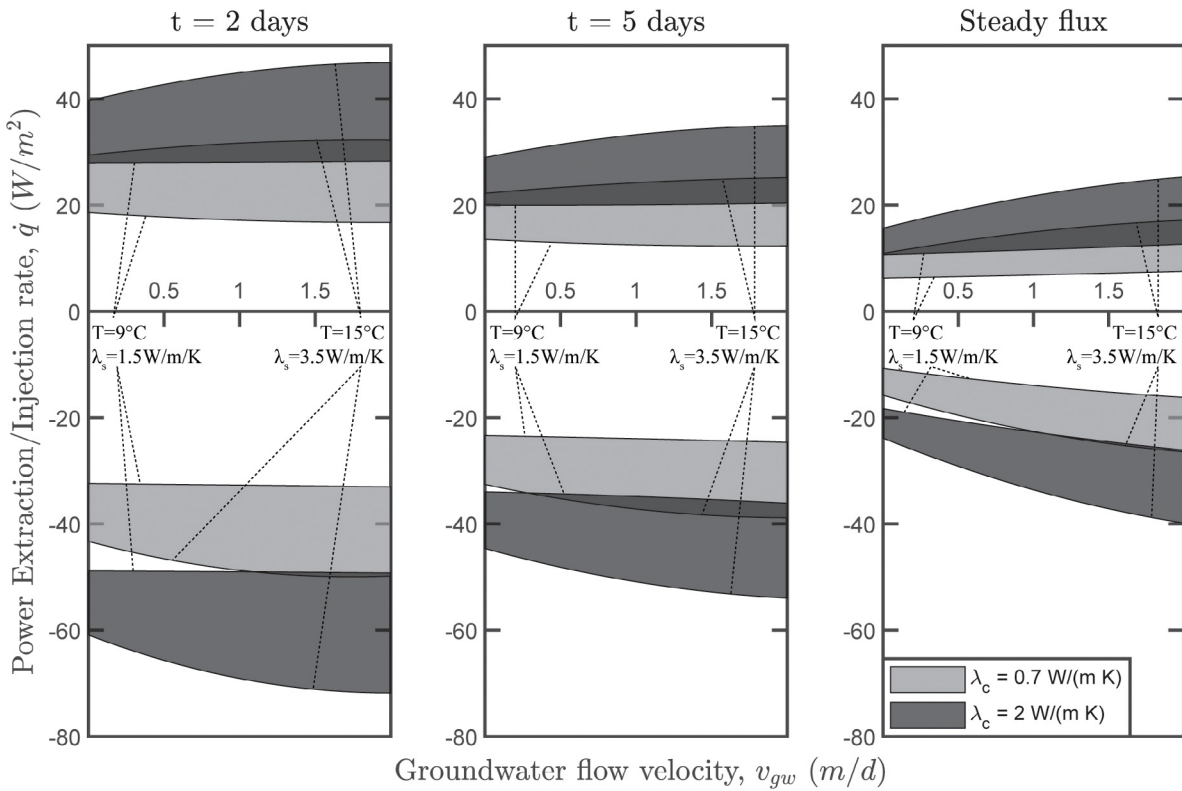
**Fig. 10.** Dependency of power extraction/injection rate on concrete thermal conductivity for groundwater flow perpendicular to the wall.

where $\overline{v}$ and $\overline{x}$ represent the velocity field and the geometrical length of the considered problem and $\alpha$ is the thermal diffusivity. For the case shown in Fig. 11(b), we have:

$$Pe = \frac{\dot{u}_x a}{2\alpha} \qquad (5)$$

This result can also be obtained by using the following ratio of times[50]:

$$\frac{1}{Pe} = \frac{time\ for\ an\ element\ in\ motion\ to\ pass\ the\ heat\ source\ of\ width\ 2a}{time\ for\ the\ heat\ to\ conduct\ a\ distance\ 2a} \qquad (6)$$

$$= \frac{t_{conv}}{t_{cond}} \begin{cases} if\ Pe \gg 1 & convective\ dominated\ problem \\ if\ Pe \ll 1 & conductive\ dominated\ problem \end{cases}$$

where $2a$ is the width of the heat source (Fig. 11(b)). Then,

$$t_{conv} = \frac{2a}{\dot{u}_x} \qquad (7)$$

and

$$t_{cond} = \frac{a^2}{\alpha} \qquad (8)$$

are obtained by invoking the approximation proposed in Ref. 51 which provides a measure of the spatial extent of the heated region based on analysis of the error function.

This knowledge can be applied to EWs by analyzing the 2D case under the following conditions. For groundwater flow parallel to the wall, the distance $2a$ can be considered as the longitudinal length of the thermo-active walls of the infrastructure (it may range between $10^0$ m and $\approx 10^3$ m), and $\dot{u}_x$ represents the magnitude of the undisturbed groundwater velocity at the wall–soil interface (ranges from 0 m/d to $\approx 2.0$ m/d). For groundwater flow perpendicular to the wall, the seepage at the wall–soil interface is directed vertically; hence the distance $2a$ can be considered as the wall height (ranges from $10^0$ m to $\approx 10^2$ m), and $\dot{u}_x$ can be considered as the magnitude of the groundwater velocity at the wall–soil interface (which is significantly lower than the undisturbed groundwater velocity ($v_u$) because of the seepage path, usually $\frac{1}{3}v_u$ to $\frac{1}{8}v_u$)[28].

In engineering applications, the Péclet number is typically large. Thus, the limit value that separates the conductive- and convective-dominated regimes must be studied for small values of the parameter $a$, which is defined as half of the length of a wall panel (e.g., diaphragm walls are usually composed of $1.5 \div 3.0$ m long adjoining concrete panels) for the case of groundwater parallel to the wall, and as half of the wall height for the case of groundwater perpendicular to the wall (Fig. 12). The thermal diffusivity was studied in the range $1 \cdot 10^{-7}$ m$^2$/s to $2 \cdot 10^{-6}$ m$^2$/s[33].

The maximum limit value of the velocity for reaching the condition $Pe < 1$ was evaluated: for the parallel groundwater flow, $v_u = \dot{u}_x \leq 0.5$ m/d. For the perpendicular groundwater flow, $\dot{u}_x \leq 0.1$ m/d, which corresponds to an undisturbed velocity of $v_u \sim (0.3 \div 0.8)$ m/d. In conclusion, a velocity value of $v_u = 0.5$ m/d can be used as a separator between the two main heat exchange modes.

*3.3.2. Flowchart for early-stage thermal performance design*
To propose a flowchart that is based on such results and theoretical principles, the conditions and implications of each heat exchange mode must be defined.

In the case of the conductive-dominated regime (i.e., when a groundwater table is not present or $v_u < 0.5$ m/d), the long-term sustainability of the project must be guaranteed. It is essential to ensure an adequate thermal recharge to the soil mass to avoid unacceptable long term temperature variations[52].
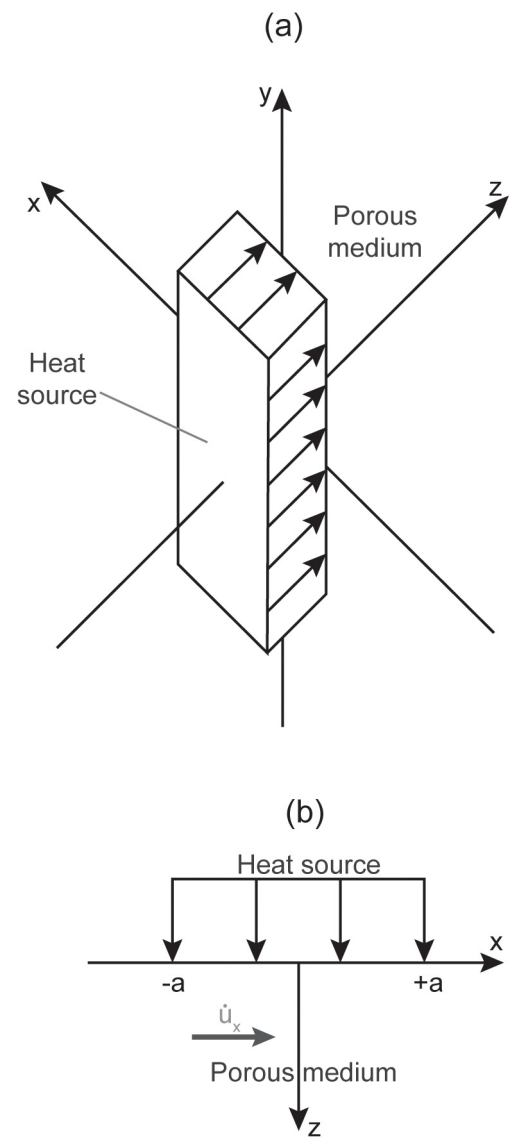


(a)

(b)

**Fig. 11.** Porous medium heated from the side, (a) 3D case and (b) 2D sketch.

In the optimum functioning mode, the cooling and heating operations are balanced. In the case of the convective-dominated regime, a designer must bear in mind that the heat storage is inhibited by the fluid flow that dissipates heat in the surrounding soil mass (i.e., only instantaneous cooling can be performed). Fig. 13 presents the flowchart that can be employed for early-stage thermal performance design.

**4. Conclusions**

This paper summarizes some concepts of hydro-thermal interactions applied to EWs and presented a methodology for the early-stage thermal performance design of such EGs.

A portion of an energy infrastructure was numerically modeled, and the thermal behavior was discussed with reference to different environmental conditions. Groundwater flow in the soil enhances the heat exchanges but induces adverse hydraulically induced thermal interactions among adjoining pipe loops. The performance of one HE loop under parallel groundwater flow conditions is higher than that for a perpendicular groundwater flow. Within this framework, the time-dependent nature of the HEs response is highlighted. The structural thermal characterization
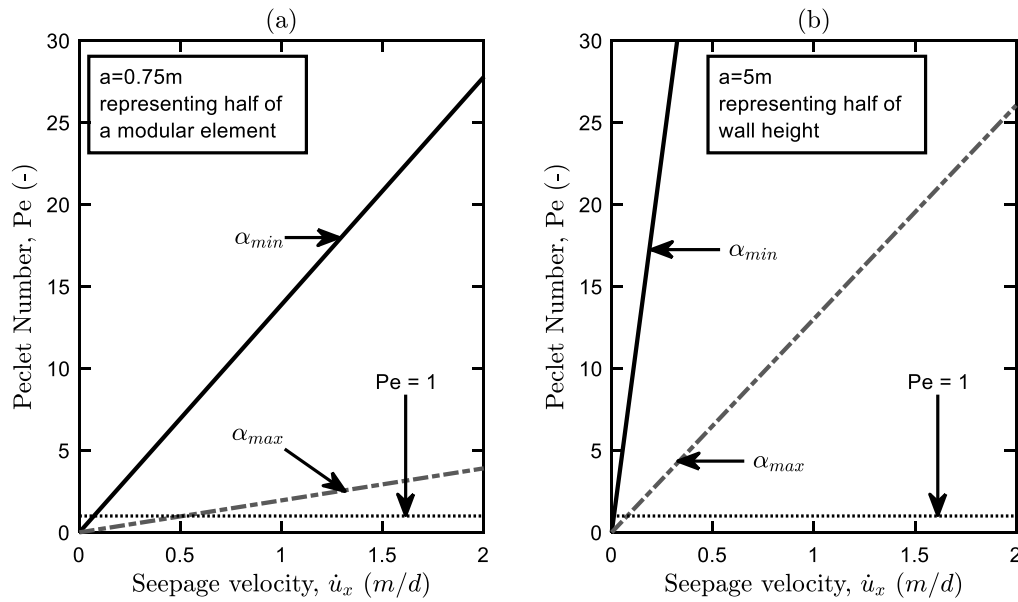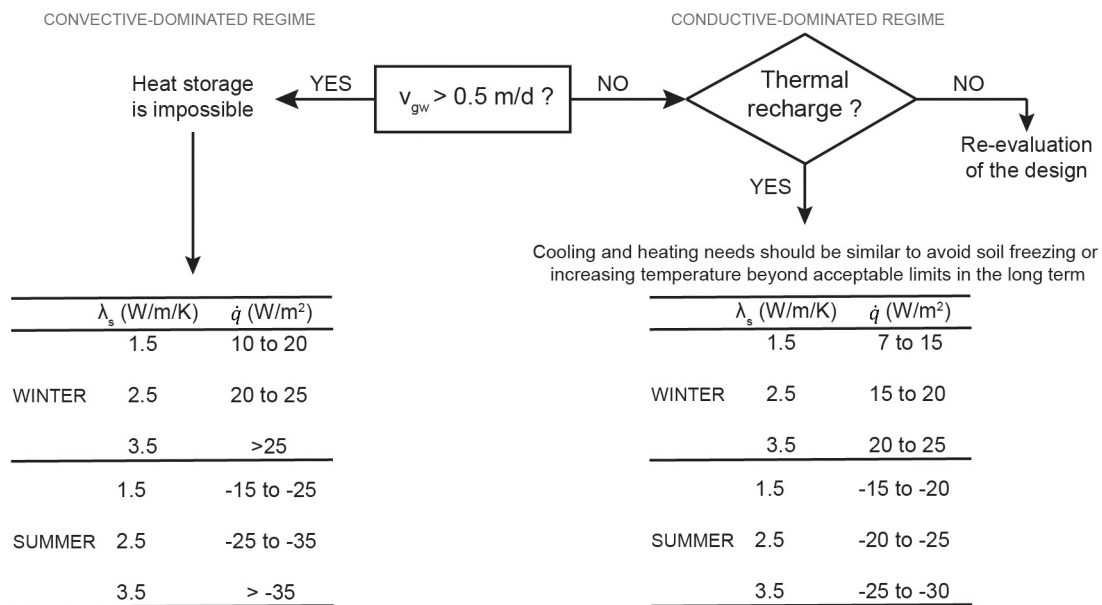
**Fig. 12.** Evaluation of the Péclet number with respect to the groundwater flow velocity for (a) parallel and (b) perpendicular groundwater flow with respect to the wall.



Additional notes:

[1] For groundwater flow parallel to the infrastructure, the power extraction/injection rate can double if the thermal interactions among adjoining pipe loops are considered and reduced by ensuring an efficient pipe layout design.

[2] Worst case scenarios (i.e. very cold climates in winter and very hot climates in summer) may affect the performance up to -35%.

**Fig. 13.** Flowchart for early-stage thermal performance design of EWs.

plays a significant role, and precise quantification of the thermal conductivity is hardly feasible, owing to the broad range of values available in the literature, the dependency on many parameters (such as the density and degree of saturation), and the long-term interactions with the soil. Consequently, the response of the HEs may vary significantly.

A methodology for early-stage thermal performance design of EWs was proposed. It has a sound theoretical basis that helps to account for the multiphysical phenomena interacting with one another (thermodynamics, fluid dynamics) at different scales. Once the basic hydro-thermal characteristics of a site are known,

the proposed flowchart can be used to determine the power extraction/injection rates expressed in W/m² of the thermo-active surface for heating and cooling operations.

This methodology will help designers to perform a preliminary quantification of the energy achievable by equipping an infrastructure with EWs during the early-stage design phases. Moreover, it may impact the decision-making process when the question is whether or not to install thermo-active elements on a planned infrastructure project. The data included in this design tool represent a conservative estimation of the power rate because of the definition of steady flux conditions with respect to the selected thermal input.

Finally, EWs exhibit considerable potential for energy exploitation. The average values for the power extraction/injection rate range between 10 W/m$^2$ and 50 W/m$^2$. The proposed early-stage thermal performance design methodology may represent a decisive tool for designers to close a gap between researchers and practitioners, enabling the EG technology to be more widely used.

## CRediT authorship contribution statement

**Jacopo Zannin:** Conceptualization, Validation, Writing - original draft, Visualization, Methodology, Software, Formal analysis, Investigation. **Alessio Ferrari:** Conceptualization, Validation, Writing - original draft, Writing - review & editing Supervision, Project administration. **Pyrène Larrey-Lassalle:** Writing - review & editing, Project administration. **Lyesse Laloui:** Validation, Writing - review & editing, Supervision, Project administration.

## Declaration of competing interest

The authors declare that they have no known competing financial interests or personal relationships that could have appeared to influence the work reported in this paper.

## Acknowledgments

## Annex A. Mathematical formulation of the numerical model

The hydro-thermal behavior is described by the following equations. The mass conservation equation of the fluid phase in the porous medium is given as:

$$\frac{\partial}{\partial t}(n\rho_w) + \text{div}(\rho_w \boldsymbol{v_{rw}}) = 0 \tag{A.1}$$

where $n$ is the porosity of the porous medium, $\rho_w$ represents the fluid density, $t$ represents the time and $\boldsymbol{v_{rw}}$ represents the fluid velocity as from Darcy's law.

$$\boldsymbol{v_{rw}} = -K\,\text{grad}\left(z + \frac{p_w}{\gamma_w}\right) \tag{A.2}$$

Here, $K$ is the hydraulic conductivity based on the hypothesis of a homogeneous porous medium, $z$ is the vertical coordinate from Fig. 1, $p_w$ is the fluid pressure, and $\gamma_w = \rho_w g$, with $g$ being the gravitational acceleration. The hydraulic conductivity, $K$, is evaluated with respect to the geometric permeability, $k^*$, $\rho_w$, $g$ and the fluid dynamic viscosity $\mu_w$.

$$K = k^* \frac{\rho_w g}{\mu_w} \tag{A.3}$$

The energy conservation equation can be separated in two parts: one related to the conductive and convective heat transfer processes in the porous materials, and another related to the hydro-thermal fluid flow inside the HEs.

The former can be expressed as follows:

$$\text{div}(\lambda\,\textbf{grad}T) = \rho C_p \frac{\partial T}{\partial t} + \rho_w C_{p,w} \boldsymbol{v_{rw}} \cdot \textbf{grad}T \tag{A.4}$$

where $\lambda$ represents the effective thermal conductivity of the materials:

$$\lambda = (1-n)\lambda_s + n\lambda_w \tag{A.5}$$

Here, the subscripts $s$ and $w$ correspond to the solid and fluid phases, respectively. $T$ is the temperature, and $\rho C_p$ represents the effective volumetric heat capacity at constant pressure:

$$\rho C_p = (1-n)\rho_s C_{p,s} + n\rho_w C_{p,w} \tag{A.6}$$

The local thermal equilibrium hypothesis is employed, which finds due justification in the literature[28,53–55].

The second part of the energy conservation equation related to the non-isothermal fluid flow inside the HEs accounts for the convective heat exchanges within the fluid and the conduction through the pipe wall:

$$\rho_f c_f A_p \frac{\partial T_{bulk,f}}{\partial t} + \rho_f c_f A_p \boldsymbol{u_f} \cdot \textbf{grad}\left(T_{bulk,f}\right) = \text{div}\left[A_p \lambda_f \textbf{grad}\left(T_{bulk,f}\right)\right] + \dot{q}_p \tag{A.7}$$

where $\rho_f$, $c_f$, $T_{bulk,f}$, $\boldsymbol{u_f}$, $\lambda_f$ represent the bulk density, specific heat at constant pressure, bulk temperature, tangential velocity, and thermal conductivity of the fluid, respectively. The cross section of the HE pipe is given as $A_p$. $\dot{q}_p$ represents the heat flux per unit length through the pipe wall, and is defined as:

$$\dot{q}_p = UP_p\left(T_{ext} - T_{bulk,f}\right) \tag{A.8}$$

where $U$ is an effective value of the pipe heat transfer coefficient accounting for the thermal resistances of the internal film and the wall. $U$ is expressed as a function of the hydraulic radius, the pipe geometry, and the thermal conductivity of the pipe material. $P_p = 2\pi r_{int}$ is the wetted perimeter of the pipe cross section, and $T_{ext}$ is the external temperature of the pipe[46,56–58].

## Annex B. Input data used to reproduce Shanghai Natural History Museum in-situ test

The input parameters used for the numerical analysis that reproduced the Shanghai in-situ test are presented in Table B.1. All the values were obtained from the publications related to such test[29,30].

**Table B.1**
Input parameters used for the reproduction of the Shanghai in-situ test.

| Description | Symbol | Unit | Value |
|---|---|---|---|
| Wall height | $H_{wall}$ | m | 38.0 |
| Excavated height | $H_{exc}$ | m | 18.5 |
| *Material properties for concrete* | | | |
| Thermal conductivity | $\lambda_c$ | W/m/K | 2.34 |
| Thermal capacity | $Cp_c$ | J/kg/K | 1046 |
| Density | $\rho_c$ | kg/m$^3$ | 2500 |
| Material properties for soil | | | |
| Thermal conductivity | $\lambda_s$ | W/m/K | 1.74 |
| Thermal capacity | $Cp_s$ | J/kg/K | 1690 |
| Density | $\rho_s$ | kg/m$^3$ | 1800 |
| *Material properties for the pipes* | | | |
| Thermal conductivity | $\lambda_s$ | W/m/K | 0.42 |
| Thermal capacity | $Cp_s$ | J/kg/K | 2300 |
| Density | $\rho_s$ | kg/m$^3$ | 950 |
| *Initial conditions* | | | |
| Wall temperature | $T_c$ | °C | 23.0 |
| Soil temperature | $T_s$ | °C | 16.3 |
| *Boundary conditions* | | | |
| Excavation temperature | $T_7 = T_8 = T_6$ | °C | 25.0 |
| Bottom temperature | $T_5$ | °C | 16.3 |
| *Thermal activation details* | | | |
| Pipe inner diameter | $d_{in}$ | mm | 25.0 |
| Pipe thickness | $t_p$ | mm | 2.3 |
| Fluid velocity | $v_f$ | m/s | 0.6 |
| Inflow fluid temperature | $T_{f,in}$ | °C | 36 |
| Pipe spacing (U-loop) | $a$ | m | 0.75 |

# References

1. Lund JW, Boyd TL. Direct utilization of geothermal energy 2015 worldwide review. *Geothermics*. 2016;60:66–93. http://dx.doi.org/10.1016/j.geothermics.2015.11.004.

2. Laloui L, Rotta Loria AF. *Analysis and Design of Energy Geostructures - 1st Edition*. Academic Press; 2019.

3. Amis T, Robinson CAW, Wong S. Integrating geothermal loops into the diaphragm walls of the Knightsbridge Palace Hotel project. In: *Proc 11th DFIEFFC Int Conf Geotech. Chall. Urban Regen.*, 2010.

4. Barla M, Di Donna A, Insana A. A novel real-scale experimental prototype of energy tunnel. *Tunn Undergr Space Technol*. 2019;87:1–14. http://dx.doi.org/10.1016/j.tust.2019.01.024.

5. Bidarmaghz A, Narsilio GA. Heat exchange mechanisms in energy tunnel systems. *Geomech Energy Environ*. 2018;16:83–95. http://dx.doi.org/10.1016/j.gete.2018.07.004.

6. Cousin B, Rotta Loria AF, Bourget A, Rognon F, Laloui L. Energy performance and economic feasibility of energy segmental linings for subway tunnels. *Tunn Undergr Space Technol*. 2019;91:102997. http://dx.doi.org/10.1016/j.tust.2019.102997.

7. Makasis N, Narsilio GA, Bidarmaghz A. A robust prediction model approach to energy geo-structure design. *Comput Geotech*. 2018;104:140–151. http://dx.doi.org/10.1016/j.compgeo.2018.08.012.

8. Mimouni T, Laloui L. Behaviour of a group of energy piles. *Can Geotech J*. 2015;52(12):1913–1929. http://dx.doi.org/10.1139/cgj-2014-0403.

9. Sailer E, Taborda DMG, Zdravkovic L, Potts DM. Numerical modelling of thermo-active shafts. In: *Energy Geotechnics*, Cham, 2019, pp. 97–104. http://dx.doi.org/10.1007/978-3-319-99670-7_13.

10. Sterpi D, Tomaselli G, Angelotti A. Energy performance of ground heat exchangers embedded in diaphragm walls: Field observations and optimization by numerical modelling. *Renew Energy*. 2020;147:2748–2760. http://dx.doi.org/10.1016/j.renene.2018.11.102.

11. Brandl H. Energy foundations and other thermo-active ground structures. *Géotechnique*. 2006;56(2):81–122. http://dx.doi.org/10.1680/geot.2006.56.2.81.

12. Brandl H. Energy piles and diaphragm walls for heat transfer from and into the ground. In: *Proc. of the Conference on Deep Foundations on Bored and Auger Piles BAP III*. 1998;37–60. Accessed: Apr. 01, 2020. [Online]. Available: http://pascal-francis.inist.fr/vibad/index.php?action=getRecordDetail&idt=6214556.

13. Laloui L, Nuth M, Vulliet L. Experimental and numerical investigations of the behaviour of a heat exchanger pile. *Int J Numer Anal Methods Geomech*. 2006;30(8):763–781. http://dx.doi.org/10.1002/nag.499.

14. Nicholson D, et al. Environmental impact calculations, life cycle cost analysis. *DFI J - J Deep Found Inst*. 2014;8(2):130–146. http://dx.doi.org/10.1179/1937525514Y.0000000009.

15. Dell R, et al. Geothermal heat in agriculture: Preliminary results of an energy intensive system in iceland. *Geotherm Resour Counc Trans*. 2011;35:8.

16. Le AT, Wang L, Wang Y, Li D. Measurement investigation on the feasibility of shallow geothermal energy for heating and cooling applied in agricultural greenhouses of Shouguang City: Ground temperature profiles and geothermal potential. *Inf Process Agric*. 2020. http://dx.doi.org/10.1016/j.inpa.2020.06.001.

17. Yang L-H, Huang B-H, Hsu C-Y, Chen S-L. Performance analysis of an earth–air heat exchanger integrated into an agricultural irrigation system for a greenhouse environmental temperature-control system. *Energy Build*. 2019;202:109381. http://dx.doi.org/10.1016/j.enbuild.2019.109381.

18. Dupray F, Li C, Laloui L. Heat-exchanger piles for the de-icing of bridges. *Acta Geotech*. 2014;9(3):413–423. http://dx.doi.org/10.1007/s11440-014-0307-2.

19. Eugster WJ. Road and bridge heating using geothermal energy. Overview and examples. In: *Proc. Eur. Geotherm. Congr. Unterhach. Ger. 30 May-1 2007*, 2007.

20. Di Donna A, Barla M, Amis T. Energy geostructures: a collection of data from real applications. In: *Wuhan China 15th IACMAG*. 2017.

21. Bourne-Webb PJ, Bodas Freitas TM, da Costa Gonçalves RA. Thermal and mechanical aspects of the response of embedded retaining walls used as shallow geothermal heat exchangers. *Energy Build*. 2016;125:130–141. http://dx.doi.org/10.1016/j.enbuild.2016.04.075.

22. Di Donna A, Cecinato F, Loveridge F, Barla M. Energy performance of diaphragm walls used as heat exchangers. *Proc Inst Civ Eng - Geotech Eng*. 2016;170(3):232–245. http://dx.doi.org/10.1680/jgeen.16.00092.

23. Loveridge F, McCartney JS, Narsilio GA, Sanchez M. Energy geostructures: A review of analysis approaches, in situ testing and model scale experiments. *Geomech Energy Environ*. 2020;22:100173. http://dx.doi.org/10.1016/j.gete.2019.100173.

24. Rui Y, Yin M. Thermo-hydro-mechanical coupling analysis of a thermo-active diaphragm wall. *Can Geotech J*. 2017;55(5):720–735. http://dx.doi.org/10.1139/cgj-2017-0158.

25. Shafagh I, Rees S, Urra Mardaras I, Curto Janó M, Polo Carbayo M. A model of a diaphragm wall ground heat exchanger. *Energies*. 2020;13(2):2. http://dx.doi.org/10.3390/en13020300.

26. Soga K, Rui Y. 7 - energy geostructures. In: Rees SJ, ed. *Advances in Ground-Source Heat Pump Systems*. Woodhead Publishing; 2016:185–221.

27. Sterpi D, Coletto A, Mauri L. Investigation on the behaviour of a thermo-active diaphragm wall by thermo-mechanical analyses. *Geomech Energy Environ*. 2017;9:1–20. http://dx.doi.org/10.1016/j.gete.2016.10.001.

28. Zannin J, Ferrari A, Pousse M, Laloui L. Hydrothermal interactions in energy walls. *Undergr Space*. 2020. http://dx.doi.org/10.1016/j.undsp.2020.02.001.

29. Xia C, Sun M, Zhang G, Xiao S, Zou Y. Experimental study on geothermal heat exchangers buried in diaphragm walls. *Energy Build*. 2012;52:50–55. http://dx.doi.org/10.1016/j.enbuild.2012.03.054.

30. Sun M, Xia C, Zhang G. Heat transfer model and design method for geothermal heat exchange tubes in diaphragm walls. *Energy Build*. 2013;61:250–259. http://dx.doi.org/10.1016/j.enbuild.2013.02.017.

31. Di Donna A. Energy walls for an underground car park. In: *25th Eur. Young Geotech. Eng. Conf.*. 2016:21–24.

32. Cornelio C, Di Donna A, Barla M. Energy diaphragm walls for Turin metro. In: *Eur. Geotherm. Congr. Strasbg. Fr.*. 2016.

33. Vulliet L, Laloui L, Zhao J. *Mécanique des Sols et des Roches (TGC Volume 18): Avec écoulements Souterrains et Transferts de Chaleur*. PPUR Presses polytechniques; 2016.

34. EN 1997 Eurocode 7: Geotechnical design. 2004.

35. Bourne-Webb P, da Costa Goncalves R. On the exploitation of ground heat using transportation infrastructure. *Procedia Eng*. 2016;143:1333–1340. http://dx.doi.org/10.1016/j.proeng.2016.06.157.

36. Peltier M, Rotta Loria AF, Lepage L, Garin E, Laloui L. Numerical investigation of the convection heat transfer driven by airflows in underground tunnels. *Appl Therm Eng*. 2019;159:113844. http://dx.doi.org/10.1016/j.applthermaleng.2019.113844.

37. Adam D. Tunnels and foundations as energy sources—Practical applications in Austria. In: *Deep Foundations on Bored and Auger Piles - BAP V*. 2008 https://www.taylorfrancis.com/ (accessed Apr. 02, 2020).

38. Brandl H, Adam D, Markiewicz R, Unterberger W, Hofinger H. Concrete absorber technology for earth-coupled concrete structures using geothermal energy for the Vienna Underground line U2 (in German). In: *Österr Ing.-Archit.-Z. 155 Jg Heft 7-92010 Heft 10-122010*. 2010.

39. I. Consulenten, Temperaturen in U-Bahnstationen. Wien. 1994.

40. IC Consulenten ZT GmbH, Wirtschaftliche Optimierung von TunnelThermie-Absorberanlagen, Grundlagenuntersuchung und Planungsleitfaden. Wien. 2005.

41. MacDonald M. Crossrail Line 1 Ventilation Requirements Review Study. London. 2004.

42. Schlosser S. Potential der tunnelbaustrecke des bahnprojektes stuttgart 21. 2007.

43. Finnish Meteorological Institute. Finnish meteorological institute. 2019 Retrieved 02 05, 2019, from https://en.ilmatieteenlaitos.fi/statistics-from-1961-onwards.

44. Servizio Meteorologico dell'Aeronautica Militare. Atlante climatico d'Italia. 2019 Retrieved 02 05, 2019, from www.meteoam.it.

45. Li M, Lai ACK. Review of analytical models for heat transfer by vertical ground heat exchangers (GHEs): A perspective of time and space scales. *Appl Energy*. 2015;151:178–191. http://dx.doi.org/10.1016/j.apenergy.2015.04.070.

46. Batini N, Rotta Loria AF, Conti P, Testi D, Grassi W, Laloui L. Energy and geotechnical behaviour of energy piles for different design solutions. *Appl Therm Eng*. 2015;86:199–213. http://dx.doi.org/10.1016/j.applthermaleng.2015.04.050.

47. Asadi I, Shafigh P, Abu Hassan ZFB, Mahyuddin NB. Thermal conductivity of concrete – A review. *J Build Eng*. 2018;20:81–93. http://dx.doi.org/10.1016/j.jobe.2018.07.002.

48. Zhang W, Min H, Gu X, Xi Y, Xing Y. Mesoscale model for thermal conductivity of concrete. *Constr Build Mater*. 2015;98:8–16. http://dx.doi.org/10.1016/j.conbuildmat.2015.08.106.

49. Valore R. Calculations of U-values of hollow concrete masonry. *Concr Int*. 1980;2:40–63.

50. Childs T, Maekawa K, Obikawa T, Yamane Y. *Metal Machining: Theory and Applications*. Butterworth-Heinemann; 2000.

51. Carslaw HS, Jaeger JC. *Conduction of Heat in Solids*. Clarendon Press; 1952.

52. Fromentin A, Pahud D, Laloui L, Moreni M. Pieux échangeurs: conception et ré de pré—dimensionnement. *Rev Fr Génie Civ*. 1999;3(6):387–421. http://dx.doi.org/10.1080/12795119.1999.9692263.

53. Nield DA. Effects of local thermal nonequilibrium in steady convective processes in a saturated porous medium: forced convection in a channel. *J Porous Media*. 1998;1:181–186.

54. Nield DA, Bejan A. *Convection in Porous Media*. Cham: Springer International Publishing; 2017.

55. Minkowycz WJ, Haji-Sheikh A, Vafai K. On departure from local thermal equilibrium in porous media due to a rapidly changing heat source: the Sparrow number. *Int J Heat Mass Transfer*. 1999;42(18):3373–3385. http://dx.doi.org/10.1016/S0017-9310(99)00043-5.

56. COMSOL Inc. COMSOL multiphysics reference manual. 2018 version 5.3. www.comsol.com.

57. Gnielinski V. New equations for heat and mass transfer in turbulent pipe and channel flow. *Int Chem Eng*. 1976;16(2):359–368.

58. Haaland SE. Simple and explicit formulas for the friction factor in turbulent pipe flow. *J Fluids Eng*. 1983;105(1):89–90. http://dx.doi.org/10.1115/1.3240948.